11.3 Detectors

11.3.1 Introduction and Effect of operating Environment

At the LHC, the signal speed, spatial resolution and granularity of silicon detectors make them a natural choice for the tracking and vertexing layers. As noted, however, at the radii of SCT detectors, the radiation exposure far exceeds that encountered by any existing tracker. Unlike the existing microvertex detectors, there is little prospect of replacing the central tracking layers during the lifetime of the experiment and maintenance access for repairs will be restricted. Given the limited experience in operating detectors after the expected radiation doses, and uncertainties in both the expected dose and the detector deterioration, the ATLAS design emphasises maximal protection against the effects of radiation (in particular stable high voltage operation and efficient charge collection in non-depleted operation), to minimise module failures over a 10 year period. By choosing to readout electrons, efficient partially depleted operation is possible after type inversion, with fast signal collection and limited charge diffusion. The collaboration is pursuing a study on the alternative of reading out holes, which potentially could offer cost savings.

Figure 1-iii and Figure 1-iv, and Table 11-3 of Section 11.2.3 show the annual neutral and charged particle fluence [11-18] estimated in the region of the SCT detectors, at a nominal 10^{41} cm^{-2} annual integrated luminosity. Including a safety factor of ~ 50 %, the total charged and neutral fluence is estimated to reach 2.14 x 10^{14} n_{eq}/cm^2 normalised by the NIEL cross-section to the damage of 1 MeV neutrons over a 10 year period. These fluences are used to evaluate the expected evolution of the operational detector characteristics.

The detector designs concentrate on features to improve the radiation tolerance. The effects of radiation are to increase the trapped charge at the surface of the devices resulting in higher electric fields and breakdown at lower voltage, and to create bulk defects which increase the leakage currents, create charge trapping and change the effective bulk doping concentration. From detector studies after irradiation, a model has been developed [11-19] for the evolution of depletion voltage V_D, bulk leakage current I_L, and charge collection efficiency ε_{eff} as a function of the radiation fluence Φ, the radiation rate $d\Phi/dt$, the radiation type, and the operational temperature T of the detector.

The value of V_D for a silicon detector of thickness d is directly related to its effective doping, N_{eff}, which is composed of ionised shallow donor levels and charged deep acceptor levels; before irradiation,

$$N_{eff} = N_D^+ - N_A^- \quad . \qquad 11\text{-}1$$

Radiation removes shallow impurities by the creation of deep donors and acceptors; since acceptor-like states predominate, the *n*-type material effectively inverts to *p*-type. The damage exhibits fast annealing that can be neglected on LHC time-scales, and a long-term change ΔN_{eff}, which depends on the fluence Φ, and one or more time constants. It is assumed that $\Delta Neff$ contains a stable part $N_C(\Phi)$, and a component $N_Y(\Phi,t,T)$ increasing with time t. $N_C(\Phi)$ can be parametrised to existing data as

$$N_C(\Phi) = N_{C0}\,(1-e^{-c\Phi}) + g_C\,\Phi \qquad 11\text{-}2$$

The values of N_{C0}, c, and g_C have been obtained by a fit to all existing data (including particle type). The reverse annealing has been parametrised assuming second order defect dynamics.

$$N_Y(\Phi,t,T) = N_{X0}\,(1-1/(1+N_{X0}(\Phi,t,T)\,k(T)\,t)) \quad , \qquad 11\text{-}3$$

with
$$N_{X0} = g_Y\,\Phi \,,$$

and
$$k(T) = k_0 \exp(-E_a/k_B T) \,.$$

The leakage current after heavy irradiation is dominated by the bulk generation of charge carriers, and this has a temperature dependence given by the Boltzman equation. The value of I_L increases by ~ a factor 2 with a 7 °C change of temperature. With fluence,

$$I_L = \alpha_{inf}\,\Phi \,, \qquad 11\text{-}4$$

but this is followed by a temperature dependent annealing. The full annealing curve can be fitted to a sum of two exponentials with the above temperature dependence, and excitation parameters E_I and E_g.

Finally, the charge collection trapping model assumes a linear graded electric field and constant charge carrier mobilities. The fit parameters are the trapping time constants τ_i for electrons and holes, such that $\frac{1}{\tau_i} = \frac{1}{\tau_o^i} + \gamma_i - \Phi$.

Parametrisations of the existing data as described in [11-19] determine the above parameters, with a statistical uncertainty which is small compared with the uncertainty in the overall fluence. The parametrisations used in the operational projections described below [11-20] are listed for completeness in Table 11-5.

Recent re-evaluations of the damage constants have resulted in a revision of the 24 GeV proton value from 0.93 to 0.58 [11-21]. Until this result is properly understood, an additional significant systematic uncertainty in V_D should be applied.

Table 11-5 Parameters used to evaluate the long term behaviour of silicon detectors in ATLAS.

Parameter	**Value**
Detector thickness	300 µm
Detector type	*n*-type bulk, N_{EFF}(initial) = 5 $10^{11}/cm^3$
g_Y	$4.60 \times 10^{-2}\ cm^{-1}$
g_C	$1.77 \times 10^{-2}\ cm^{-1}$
k_0	$520\ cm^3/s$
E_a	1.31 eV
N_{C0}	$1.96 \times 10^{11}\ cm^{-3}$
c	$2.29 \times 10^{-13}\ cm^2$
α_{inf}	2.86×10^{-17} A/cm
E_I	1.09 eV
E_g	1.24 eV
γ_e	$0.24 \times 10^{-6}\ cm^2/s$
γ_{e*}	$1.01 \times 10^{-6}\ cm^2/s$
γ_h	$0.24 \times 10^{-6}\ cm^2/s$

Because of the sensitivity of the depletion voltage to the operating and storage temperature, a realistic access scenario must be developed. Figure 11-4 shows the development of V_D as a function of time, assuming several access and warm-up scenarios, and an integrated fluence close to the maximum expected for the SCT. A detector thickness of 300 µm is assumed. Assuming conservatively that the detector is removed each year for maintenance, a 'standard access procedure' (SAP) has been defined. The detector has been designed assuming an operational temperature of -7 °C, a warm-up time of 2 days at 20 °C, and a 14 day maintenance period at 17 °C. The effect of different operating temperatures, assuming SAP, is shown for the range of expected V_D in Figure 11-5. An operating temperature of -7 °C has been chosen, to minimise the detector V_D increase from long term annealing.

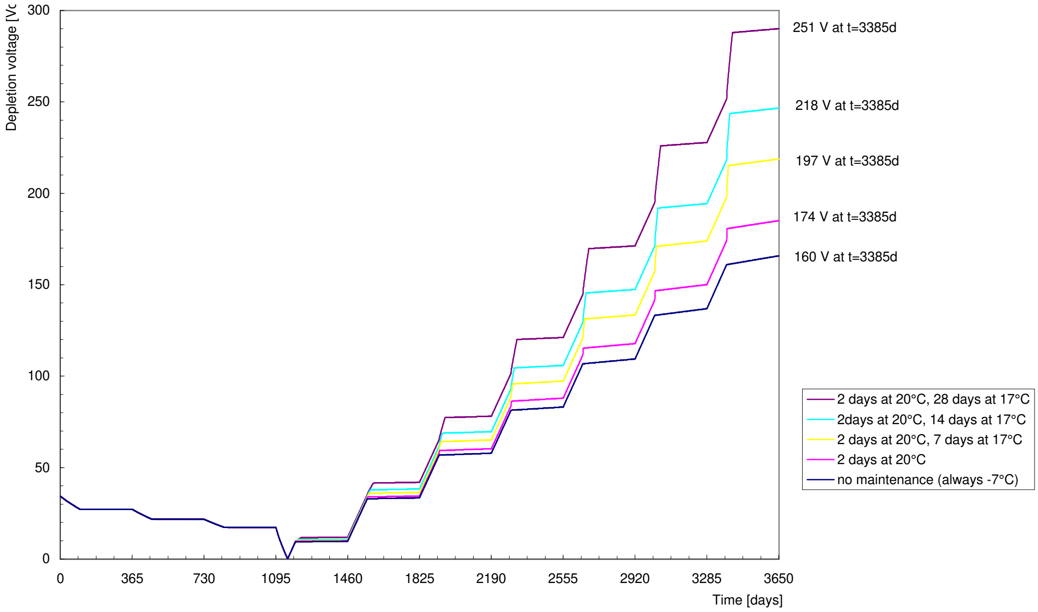

Figure 11-4 Dependence of detector depletion voltage V_D as a function of time, assuming an integrated fluence after 10 years of 1.4 x 10^{14} n_{eq}/cm^2, and an operating temperature of -7 °C. Different access scenarios are assumed as annotated. The standard access procedure assumed for the SCT design is an annual warm-up of 2 days at 20 °C, and 14 days at 17 °C. The detector thickness is assumed to be 300 µm.

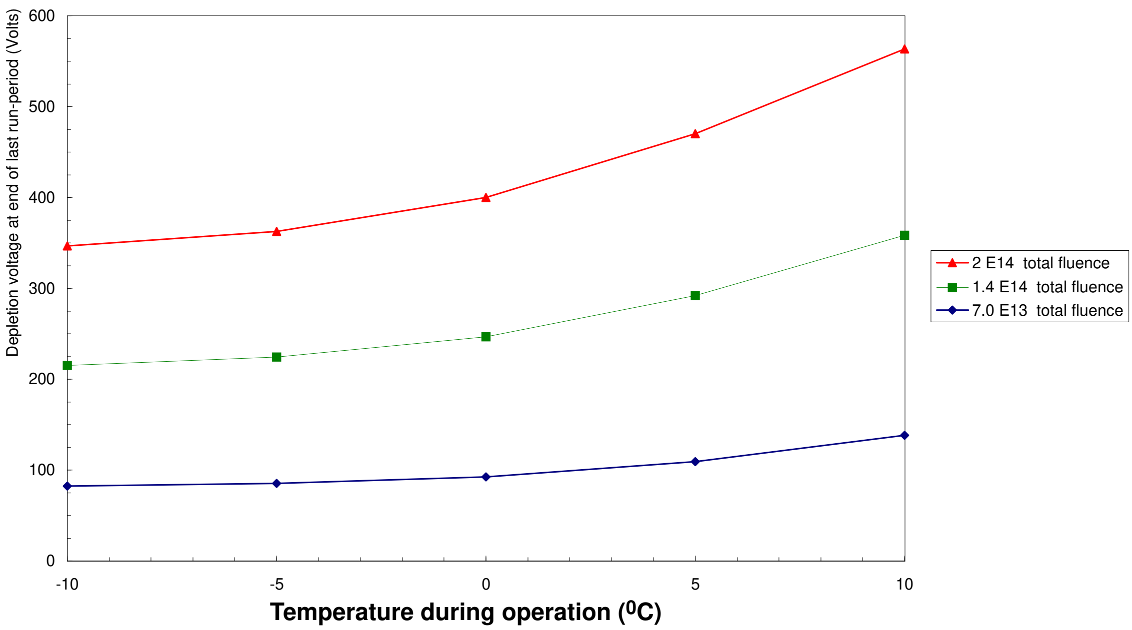

Figure 11-5 Dependence of V_D on operating temperature for several integrated fluence values, assuming an annual warm-up period of 2 days at 20 °C, and 14 days at 17 °C. The detector thickness is assumed to be 300 µm.

Table 11-6 Expected depletion voltage V_D for each barrel module type, due to the expected fluence Φ at ATLAS. Also listed are results for a 50% larger fluence. The assumed access scenario is described in the text (SAP)

	V_D (volts)	V_D (volts) 1.5 x Φ	V_D (volts)	V_D (volts) 1.5 x Φ
	z=0 cm		z=75 cm	
Barrel 1	218	381	224	390
Barrel 2	150	265	161	284
Barrel 3	124	219	122	217
Barrel 4	95	171	106	189

Table 11-7 Expected maximum depletion voltage V_D for each disk module type, due to the expected fluence Φ at ATLAS. Also listed are results for a 50% larger fluence. The assumed access scenario is described in the text (SAP).

		V_D (volts)			V_D (volts) for 1.5 x Φ	
	Inner	Middle	Outer	Inner	Middle	Outer
Disk 1	255	208	136	444	364	240
Disk 2	-	179	122	-	315	217
Disk 3	238	176	118	414	309	209
Disk 4	222	186	116	387	326	206
Disk 5	234	188	130	408	329	230
Disk 6	245	183	128	426	320	227
Disk 7	-	201	147	-	352	259
Disk 8	-	206	179	-	361	315
Disk 9	-	-	210	-	-	366

Table 11-8 Maximum expected detector leakage current I_L due to bulk damage, and minimum charge collection efficiency $\mathcal{E}_{COLL}$ for detectors in each barrel, and each disk module type. In the case of (†), I_L is projected for an undepleted operating voltage of 300 V. The SAP access scenario is assumed.

	Max. bulk I_L per detector (μA)		Min $\mathcal{E}_{COLL}$ (%)	
	Φ_{exp}	1.5 x Φ_{exp}	Φ_{exp}	1.5 x Φ_{exp}
Barrel 1	315	470†	92	79†
Barrel 2	250	375	92	90
Barrel 3	210	310	92	92
Barrel 4	190	280	92	92
Disk 1 Inner	315	470†	91	74†
Disk 1 Middle	280	420†	92	81†
Disk 9 Outer	285	425†	92	80†

Table 11-6 and Table 11-7 list the projected V_D for module operation at extreme positions of each barrel layer, assuming the fluences discussed in Table 11-3 and Table 11-4 of Section 11.2.3. In the most pessimistic case, the detector V_D does not exceed 450V; this means that even in this scenario the operation at 300 V of *n*-in-*n* detector designs described in this Section will meet the LHC requirements. The maximum detector leakage currents at an operating temperature of -7 °C and the SAP access scenario is listed in Table 11-8. In no case will the bulk detector current for a module exceed 2 mA. It is emphasised, however, that surface contributions and guard ring currents will increase the effective I_L for the module. Also shown in Table 11-8 is the predicted charge collection efficiency ε_{COLL} for each module type. At operating voltages not exceeding 300 V in the most pessimistic operating scenario, ε_{COLL} remains adequate. Detectors of the *n*-side readout design have been tested after $2x10^{14}$ protons/cm^2 and data with these detectors have been accumulated using LHC readout electronics as described in Section 11.4. Radiation studies using devices from a range of manufacturers are continuing; results show a signal:noise (S/N) ratio of ≥ 15 for a 12 cm silicon strip length using detectors of the ATLAS design as discussed in Section 11.3.4.

11.3.2 Specifications

The tracker design requires one rectangular 'barrel' detector design and five slightly different designs for the wedge shaped 'forward' detectors which are to be built into disks. The specifications discussed here [11-22] are for barrel detectors but apply to all the designs except for the required geometrical differences.

After the anticipated radiation doses, all the strip detectors are expected to have significantly changed their device properties. Bulk damage will have altered the detectors' depletion characteristics with the charge collection region growing from the *n*- implant side with bias voltage. Surface damage will have raised the oxide-silicon interface charge by an order of magnitude and designs need to balance the requirements of low capacitance with those of avoiding high field regions and possible breakdown.

In the specifications below, issues for the mask design are separated from the device properties (which give the device performance which each detector must fulfil) and the requirements, which are design goals which are necessary, but not testable on a device-by-device basis. The discussion on processing reflects current knowledge of how operational requirements in the severe radiation environment at the LHC may be met. Processing techniques to improve the high voltage performance are under discussion with manufacturers.

11.3.2.1 Detector mask specifications

Figure 11-6 shows, for a barrel detector, the overall device layout and locations of bias contacts, bond pads, alignment features, identification marks, etc.

- The barrel device size is 64 x 63.6 mm^2 cutting scribe line to cutting scribe line, with a sensitive region 62x61.6 mm^2. Optimisation is for 4″ wafers.
- A total of 768+2 (768 read out) strips exist with implant strip dimensions 18µm wide, 62mm long, 80µm pitch, high doped *n*-implant.

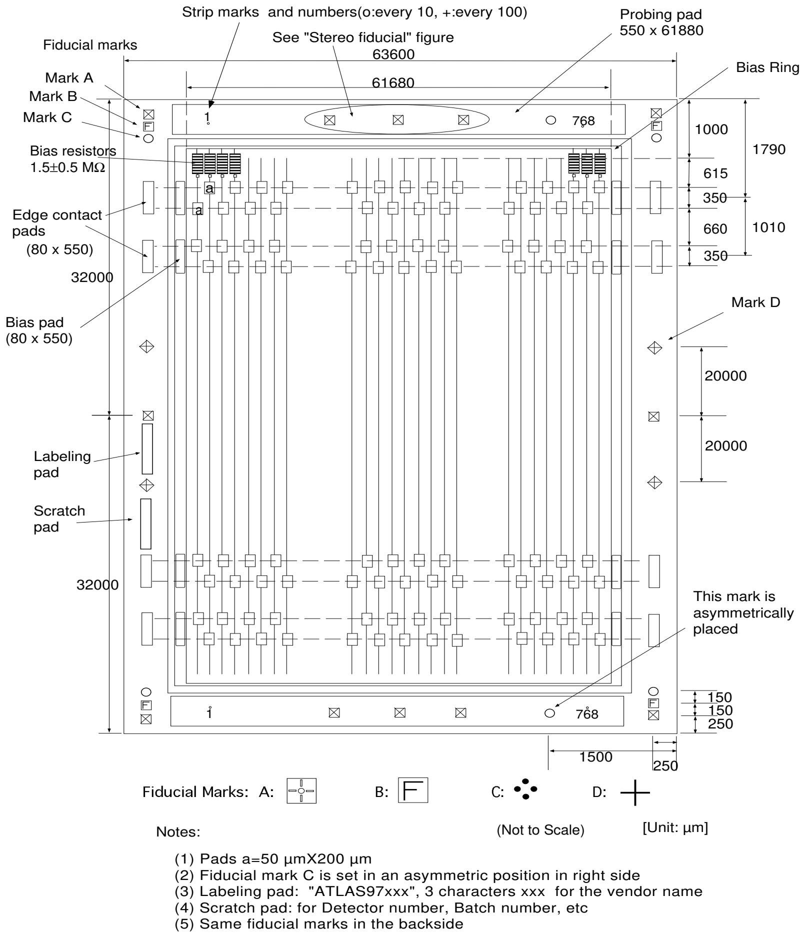

Figure 11-6 Mask design and bond layout of the SCT Barrel Detector.

- The readout strips are aluminium, capacitively coupled over the *n*-implant strips with a processed aluminium edge >1µm everywhere within the processed boundary of the implant strips. The capacitance and metal resistance requirements imply that these gaps should be as close to 1µm as mask alignment tolerances etc allow.
- The isolation technique uses individual *p*-stops with implanted *p*-strips normally of 17µm width. The gaps between the *p*-implants are >6 µm and the nominal distance in the device between n- and p-structures is > 10 µm. The requirement of no *p*-implant below the bond pads requires that the width of the implanted *p*-stop lines reduces to 8µm in this region. Figure 11-7 shows the layout required in the bond pad region.

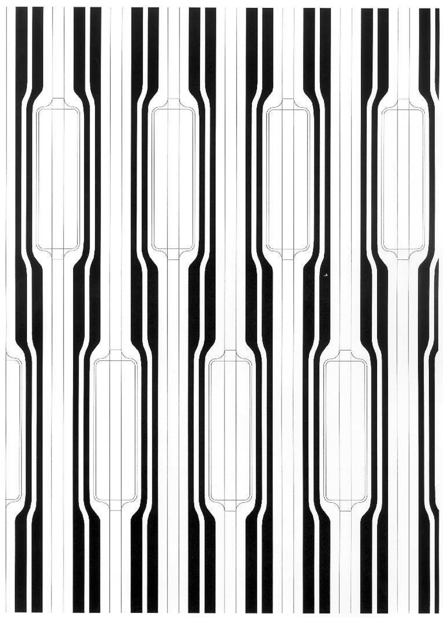

Figure 11-7 Details of the detector layout in the bond pad region.

- The bias resistors overlap the implanted strips or are contained within the guard ring region.
- The distance between the sensitive region and the cut edge is 1mm.
- The distance between the outermost guard and the cut edge is > 500 µm.
- On the back side, contactable *p*-implants match the *n*-implant dimensions up to first guard. *p*-side guard rings are contacted to aluminium over the implants. The *n*-side has both *n*- and *p*-implanted guard rings. Only the *n*-type guard rings are contacted to overlapping aluminium rings. Figure 11-8 (adjacent to bond pads) and Figure 11-9 (corner region) show one proposed design.
- There are 200 x 56 µm^2 readout bond pads, in two rows, and daisy-chainable (see Figure 11-6)
- The *n*-bias contacts are available at each corner (see Figure 11-6).
- To enable strip evaluation probe points to readout strip implants exist at the contact point to the bias resistors.
- The detectors are passivated on both sides using silicon oxide.
- Every 10th strip is clearly numbered, with scratch pads used for detector labelling and alignment marks for module optical metrology (see Figure 11-6).

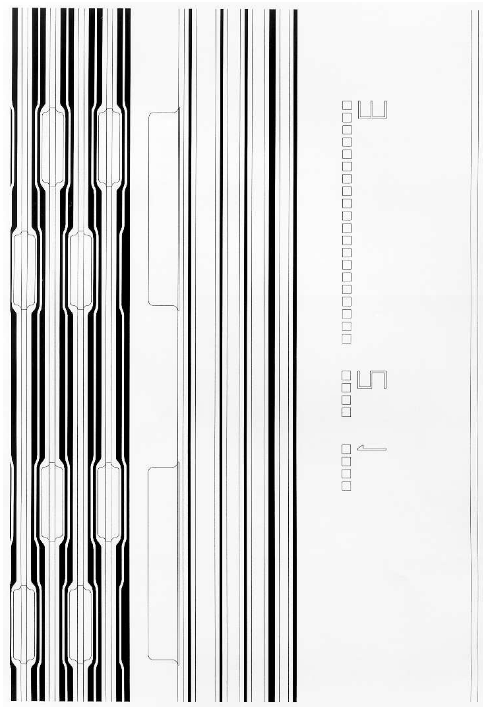

Figure 11-8 Strip layout adjacent to bond pads.

Figure 11-9 Strip layout in corner region.

11.3.2.2 Mechanical and optical specifications

The detector mechanical and optical specifications are described below:

- External cut dimensions are 64 x 63.6mm^2 with ±25 µm tolerance; edge chipping must be avoided.
- The thickness is 300 ±15 µm, with thickness uniformity ±10 µm.
- A mask alignment tolerance of < 3µm with respect to any other mask is required.

11.3.2.3 Detector electrical specifications

The detector electrical specifications are described below:

- The strip *n*-implant is <200 KΩ/cm.
- The aluminium readout strips satisfy a resistance of <20 Ω/cm.
- The bias resistance satisfies 1.5±0.5 MΩ polysilicon bias.
- $C_{coupling}$ > 10 pF/cm
- The depletion voltage is required to satisfy V_D< 100V.
- The total initial leakage including guard is required to be I_L< 6μA at 150V and I_L< 20μA at 200V. An increase in I_L by < 2μA after 24 hours in dry air is required to establish stability.
- The processing reproducibility is monitored on test structures (V_{FB}, t_{ox}, implant and polysilicon resistivity, aluminium sheet resistance, etching uniformity, dielectric strength etc). To check the dielectric integrity I_L < 1nA/cm^2 after 1 hour at 100V measured on large area test structures is required. This is needed to ensure adequate protection against `beam splashes' occurring when the detector is being operated at high voltage.

11.3.2.4 Bad strip quality specifications

Detectors may suffer bad strips because of defective strips, or from the polysilicon connection (the strip connection to bias via polysilicon broken).

- Each aluminium strip is to be contacted with a probe to check for no shorts through the coupling dielectric at 50V. Other defects may include metal/diode breaks or shorts to neighbours or broken polysilicon contact.
- A mean strip acceptance per detector of 99% in each delivery with no devices below 98% is required.

11.3.2.5 Detector performance and processing specifications

Each detector must satisfy the additional requirements listed below before and after irradiation at the corresponding maximum operating voltages. However, these criteria cannot be checked on a detector by detector basis.Therefore delivered prototypes of the same design and processing as the production delivery are required to satisfy these conditions.

- The maximum operating voltage is 150V initial, and 300V after the equivalent of ~2 x 10^{14} 24 GeV protons/cm^2
- It is required that $R_{inter-strip}$ > 2 x R_{bias} at the maximum operating voltage.
- $C_{Total-Load}$ < 1.2 pF/cm at maximum operating voltage.
- The strip current I_L< 1μA per readout strip at -10 °C and 300V after the equivalent of 2 x 10^{14} protons/cm^2, and I_L < 50 nA at 150V prior to irradiation.
- The total current I_L < 1 mA at -10 °C and 300V after the equivalent of 2 x 10^{14} protons/cm^2.
- No excess noise due to micro-discharge should exist at the maximum operating voltage. (this can only be checked after connection to electronics).

- After irradiation, the number of strips failing the pre-irradiation criteria should remain within the pre-irradiation acceptances.

The aim of these specifications is to safely satisfy the performance requirements; consequently the processing steps below are required (alternative solutions proven to 2×10^{14} protons/cm^2 will also be considered).

- The *n*-implant is > 10^{14} cm^{-2} and of 1-1.5μm implant depth.
- The strip capacitor dielectric is made from silicon oxide and silicon nitride layers.
- The back contact *p*-implant is of a level > 10^{14} cm^{-2}.
- The Isolation *p*-stops have a doping level > 10^{13} cm^{-2} with the doping maximum near the oxide interface.
- The substrate doping is *n*-type with resistivity range 3 KΩcm < ρ < 8 KΩcm.
- The substrate oxygen concentration is typically 5×10^{15} cm^{-3} and < 10^{16} cm^{-3}.
- The substrate carbon concentrations is typically 5×10^{15} cm^{-3} and < 2×10^{16} cm^{-3}.

11.3.3 Discussion of Technology Choices

The parameters described in the specifications have evolved from prototyping studies within ATLAS, in the DRDC collaborations RD2 and RD20, and from the SSC. Prototyping has involved Micron Semiconductor [11-23], Hamamatsu [11-24], CSEM [11-25], Sintef [11-26], MPI [11-27] and MSU [11-28]. Results with detectors from these manufacturers are discussed below in Section 11.3.4 and many of the measurements influencing the final designs are also presented.

The dimensions of the individual barrel silicon wafers are 64 x 63.6mm^2, this being the largest usable area on a 4″ wafer. The detectors for the forward regions require a slightly different geometry to give radial strips when mounted on forward disks. Figure 11-10 shows the mask design for one such detector.

A negative bias is supplied to a large-area lithographically defined p-implant on the back of the detectors and this is surrounded by guard rings to step down the voltage towards the edge of the device, and to interrupt surface currents. The detectors consist of high resistivity (>3KΩcm) silicon and are run at an initial bias voltage sufficient to deplete the 300μm thickness of the wafers (typically 50-100V). Care is needed in the designs of the edge region to allow for the higher voltage operation required after heavy irradiation. The *n*-side guard ring design is also required to give optimal high voltage performance after irradiation.

The choice of *n*-strip readout, as already discussed, is to allow readout from the face which effectively becomes the junction after type inversion with the depleted region growing from the *n*-side. The sensitive region grows from this surface after irradiation as $\sqrt{V}$ as is borne out by data of Section 11.3.4. The use of *n*-strip readout then allows operation with high efficiency well below the final depletion voltage required after severe irradiation as discussed below. Studies with *p*-side readout show that signals can be seen below depletion but that they are broader and therefore give a lower efficiency with a single-strip threshold.

The detectors are capacitively-coupled with polysilicon biasing and have readout on every implanted strip. The choice of polysilicon biasing is motivated by the deteriorated noise performance of reach-through biased detectors after irradiation (see Figure 11-30 below). The resistor

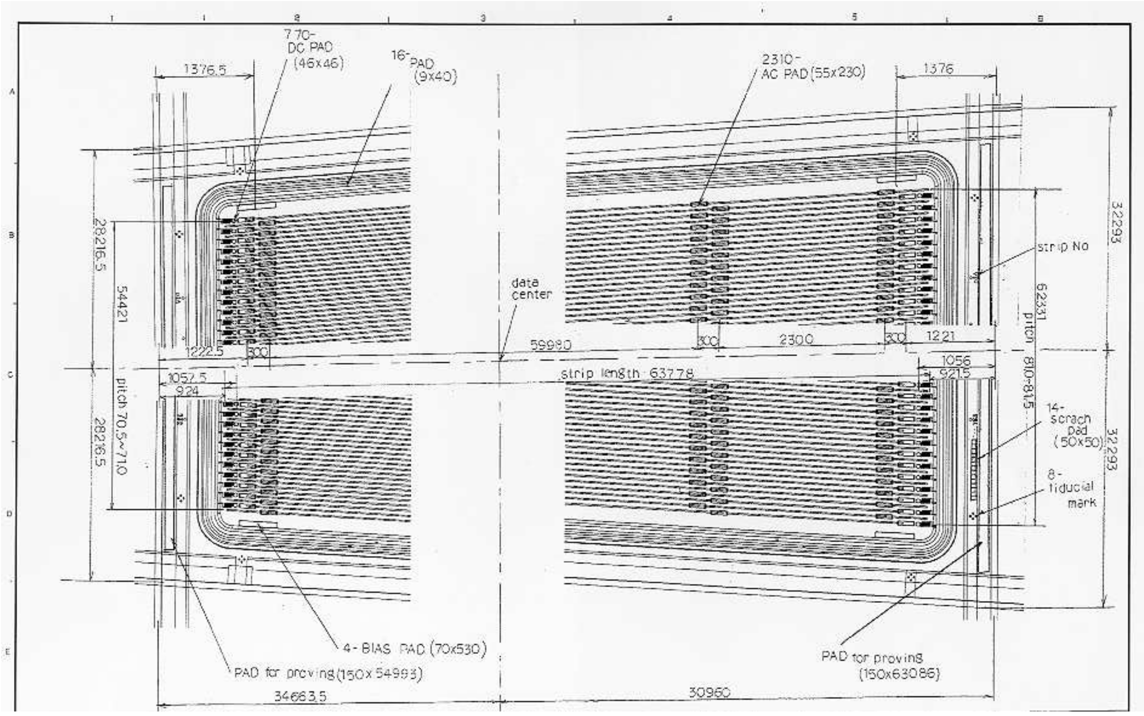

Figure 11-10 Mask design and bonding pad layout for the ATLAS SCT forward detector.

values chosen are the lowest possible, consistent with no significant increase of readout noise, to keep voltage drops to a minimum at the final I_L values. Individual strip readout suppresses charge division as required given that the baseline electronics has a single strip threshold.

The capacitive dielectric is a dual layer of nitride and oxide; this reduces the sensitivity to photolithographic faults in a single layer and provides much greater robustness against dielectric breakdown. In the absence of charge division the thickness specification of the coupling dielectric is that the coupling capacitance is significantly larger than the inter-strip capacitance. The implant and aluminium strip dimensions have been chosen experimentally on considerations of 'micro-discharge' (see Figure 11-26 below) [11-34].

The choice of individual *p*-stop has also been driven by these studies and results on irradiated detectors suggesting a slightly lower noise (and capacitance) than the continuous p-stop options.

Figure 11-11 shows a photograph of the corner of a wedge shaped detector which has 5 metalised guard rings on the *n*-side (the first also serving as the bias rail) inter-spaced with *p*-implanted guard rings. The physical edge of

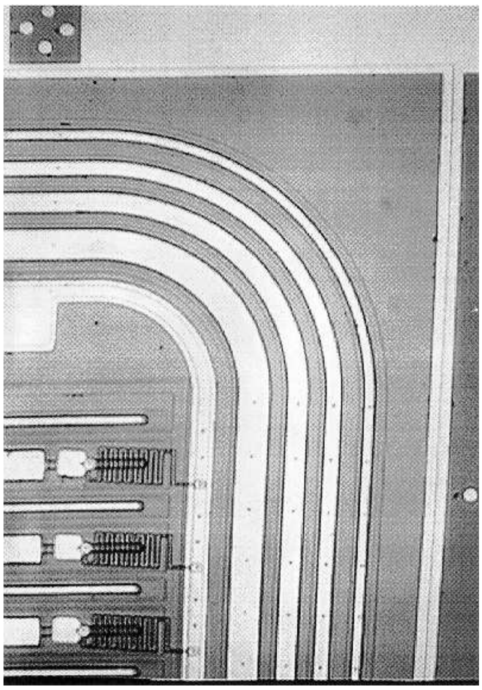

Figure 11-11 Corner photograph of a wedge detector.

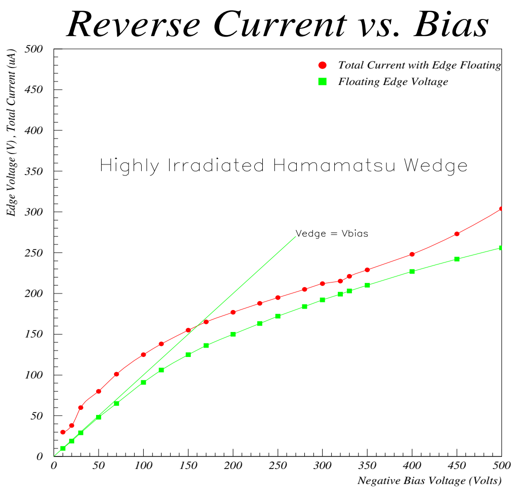

Figure 11-12 Edge voltage and total current versus bias with no voltage (i.e. floating) applied to the edge contact.

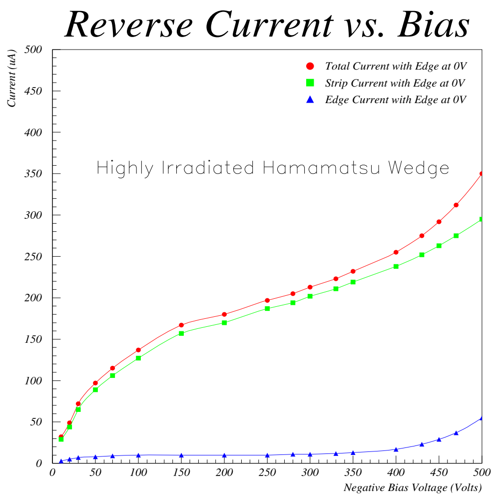

Figure 11-13 Total strip and edge current versus bias, with 0 V applied to the edge contact.

the device has a metalised *n*-implant on both faces of the detector. On the back of the detector the *p*-implanted guard rings mirror the *n*-implanted rings. The metallisation over the guard rings is contacted to the implants and it overlaps the edges of the implanted regions. Figure 11-12 shows that with this design, the voltage at the physical edge of the detector (measured by contacting the metalised *n*-implant there) tends towards the mid-voltage between the two faces for a highly irradiated (2 x 10^{14} protons/cm^2) detector run at up to 500V. The I-V curves of Figure 11-13 show that very little current in this design is taken by the edge region.

On the detector of Figure 11-11, the polysilicon resistors are run over the end of the implanted *n*-strips. The isolation structure, an individual *p*-stop around each *n*-strip, is also clearly visible. This is the current choice of isolation technique although some others are still being investigated. The detector differs from the final specifications as the width of the aluminium is 6µm narrower than the *n*-implant and this is now known to be unnecessary. By matching the aluminium width on the mask to the implant width, the resistance and hence the series noise of the metal strip can be reduced. Data using binary readout electronics with an *n*-in-*n* AC-coupled barrel detector of 80µm pitch (the nomenclature used is nn80AC) show a noise improvement when the strip width is increased.

11.3.4 Prototype Performance before and after Irradiation

The SCT collaboration has prototyped full-sized detectors from several manufacturers. Designs have evolved to follow the detector decisions taken by the SCT, and prototype data from the detectors have provided essential input to these decisions.

The *n*-in-*n* detectors designed in 1995 had dimensions 60 x 60 mm^2 and were produced for binary electronics with 75µm readout pitch, or for analogue systems with 112.5 µm readout pitch and intermediate charge-division *n*-implant strips. Both individual *p*-stops and continuous *p*-frames were prototyped to provide the isolation between the *n*-implant strips, and varying guard-ring and field-plate structures were employed with the different manufacturers for edge termination. All single sided detector designs discussed in this report used polysilicon resistors for the biasing technique.

The external barrel detector dimensions are now fixed to be 64 x 63.6 mm^2 and the readout pitch at 80 μm. A barrel detector of this design, and wedge detectors for the forward SCT, were prototyped in 1996. For 1997, final prototypes to the agreed specification and design are being planned.

Parameters of the *n*-in-*n* detectors for which results are presented are summarised in Table 11-9. Region 2 of barrel detector C and the wedge detector D are close to the final prototype design of 1997, as specified in Section 11.3.2.2.

Table 11-9 Some parameters of the *n-**in**-n* detectors for which results are presented.

Label	Area mm^2 Thickness (μm)	Pitch (μm)	Charge division strips	Individual p-stops	Common p-frame	Terminatio n: multiple guard	Terminatio n: Field plate	Fabricant
A	60x60 300	75	0	Y		Y		CSEM [11-25]
B	60x60 300	75	0		Y		Y	Hamamatsu [11-24]
C	64x63.6 300	80	0	Y	Y		Y	Hamamatsu [11-24]
D	Wedge 300	~80	0	Y		Y		Hamamatsu [11-24]
E	60x60 280	112.5	1	Y		Y		SINTEF [11-26]

Detector C was made with six different regions of *p*-stop design and metallisation readout strip width, as indicated in Table 11-10, to allow a direct comparison of the corresponding detector performances and properties. A common *p*-stop structure is sufficient to cancel oxide charge but will capacitively couple strips across the entire detector. An alternative is individual *p*-stops around each strip. This configuration will however leave an accumulation layer between strips which again either couples strips across the detector or contributes to extra charge division. The situation may be improved by adding a narrow line of 'common' *p*-stop between the 'individual' *p*-stop lines to eliminate the conductive accumulation layer. The last structure is referred to as the 'combined' *p*-stop.

For all the detectors listed in Table 11-9, measurements were made on unirradiated prototypes, and on detectors that have been exposed uniformly to 24 GeV proton irradiation at the CERN PS, with proton fluences of up to 2 x 10^{14} protons/cm^2. Results from laboratory measurements of capacitance, metal strip resistance and detector current before and after irradiation are presented. Detectors have also been attached to LHC-speed analogue electronics for measurements of noise, of the charge collected from minimum-ionising particles (from a ^{106}Ru source) and of strip readout quality both before and after irradiation. Some detectors have been constructed into modules, and the combined performance of the detector and electronics measured in test beams at CERN and at KEK. These test beam results are described in detail in Section 11.5; aspects directly related to the detector design are noted below.

In parallel with the work on single-sided detectors during 1995 and 1996, double sided detector prototypes were developed incorporating reach-through, rather than polysilicon biasing on both sides, and *p*-spray isolation between the *n*-side readout strips. The number of processing steps was minimised and the design emphasised the high-voltage performance of detectors after irradiation. Data from these devices that address the choice of biasing technique and detector performance after irradiation are also included in this section.

Table 11-10 Patterns of *p*-isolation implants between the *n*-strips and metal widths in the 6 different regions of C. Each region covers 128 readout strips.

Region	Metal width (μm)	p-isolation type	Widths of *n*- and *p*- implants and gaps (μm)							
			n	gap	p	gap	p	gap	p	gap
1	16	slit-common	16	10	18	8	18	10	-	-
2	16	individual	16	10	18	8	18	10	-	-
3	16	combined	16	10	11	6	10	6	11	10
4	16	full-common	16	10	44	10	-	-	-	-
5	22	full-common	16	10	44	10	-	-	-	-
6	10	full-common	16	10	44	10	-	-	-	-

11.3.4.1 Interstrip capacitance and aluminium strip resistance

The baseline detectors are designed to have a good noise performance while maintaining a sufficiently low field strength within the detector to operate without breakdown at 300V after irradiation. Low values for the interstrip capacitance and metal readout strip resistance are required

The total capacitive load is specified as <1.2 $pFcm^{-1}$, and the aluminium strip resistance as <20Ωcm^{-1}. Figure 11-14 shows, as an example, the interstrip capacitance, measured between one strip and its five neighbours on each side, for regions 2, 3 and 4 of the detector C. All values are within specification, with the designs including individual *p*-stops giving somewhat lower results. Similar values are measured on the other binary readout-pitch detectors prototyped.

From one manufacturer (Hamamatsu), values as low as 11Ωcm^{-1} have been measured with the 16μm metal width chosen for ATLAS by the use of pure aluminium strips. This is well within specifications.

11.3.4.2 Detector irradiation at the CERN PS

Batches of between 10 and 30 of each of the prototype detectors listed in Table 11-9 have been received, and between two and four detectors of each type have been irradiated in a 24 GeV proton beam at the CERN PS during 1996. The damage normalisation to 1 MeV neutrons is assumed to be 0.58 (see Section 11.2.3).

Each detector was mounted by its corners on a ceramic board and the readout strips and *n*-side guard rings were bonded to aluminium tracks on a glass pitch adapter which were grounded during the irradiation. Before and after irradiation the detector was connected to an analogue readout chip by bonding to the same pitch adapter, as described in Section 11.3.4.5 below. A constant bias voltage of 150 V was applied across each detector throughout its irradiation, and the detectors were maintained at an average temperature of approximately -10 °C by the circulation of cold nitrogen gas through their insulated container. The box was scanned through the

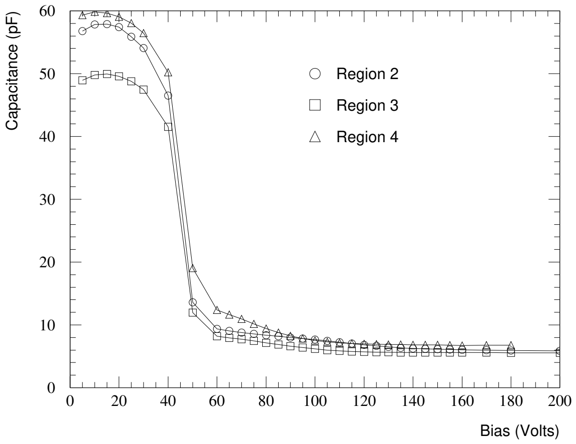

Figure 11-14 Interstrip capacitance as a function of detector bias for regions 2, 3 and 4 of detector C. The strip length for this detector is 6.2cm.

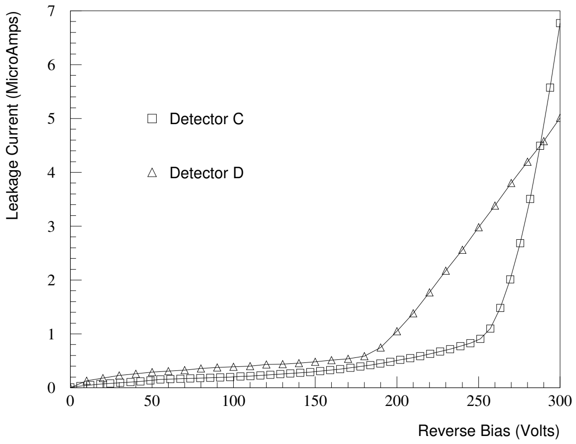

Figure 11-15 Pre-irradiation I-V curves for detectors C and D**.** Measurements have been made in air at 18.5 °C.

24 GeV proton beam to ensure uniform irradiation across the whole detector area. The temperature and the detector currents were monitored throughout the irradiation.

Most detectors received a dose of 2×10^{14} protons/cm^2 over an ~10 day period in a 24 GeV beam. A few detectors were removed after a dose of 7.6×10^{13} protons/cm^2. All detectors have been kept at low temperature, ≤ -10 °C following their irradiation, apart from a few hours of warm-up for bonding the pitch-adapter to the readout system, and for transport to outside institutes for measurement. The data therefore correspond to detector properties before the onset of reverse annealing.

11.3.4.3 Detector I-V characteristics before and after irradiation

The current-voltage characteristics of the unirradiated detectors were measured up to a detector bias of at least 250V. Figure 11-15 shows a typical result for detectors of type C and D, measured at room temperature. The currents are very stable with time, both in air and in nitrogen, and their values are well below the pre-irradiation specifications of <6 μA at 150 V and <20 μA at 200 V. Figure 11-16 (a) and (b) show the I-V curves for various *n*-in-*n* detectors after irradiation to a fluence of 2×10^{14} protons/cm^2, the measurements being made at temperatures of -10 °C and -15 °C respectively. Before these measurements were taken the detectors had all at some point been warmed up to room temperature for a period of a few hours. It is seen that the detector types described in this report perform satisfactorily up to about 300V. Their currents at 300V are all of a similar magnitude, < 500 μA when normalised to a temperature of -10 °C. The corresponding specification limit on the current is 1 mA, and so the performance of the prototype *n*-in-*n* detectors is satisfactory. All currents are stable with time.

The plots of Figure 11-17 shows the relative current in the bulk and guard regions for the irradiated detectors A, C and E. The data were taken under different operating conditions, but nevertheless provide an indication of the relative bulk and guard currents in these detectors. In particular, the increased detector A current in Figure 11-16 above 200 V is likely to result from the guard region.

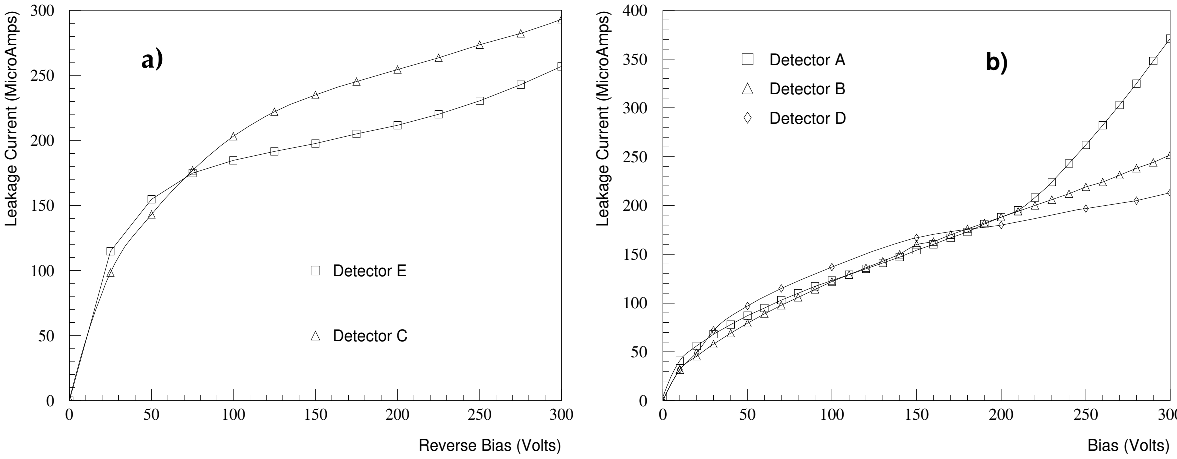

Figure 11-16 (a) I-V curves measured at -10 °C for detectors C and E after irradiation by 2x10^{14} protons/cm^2 in a 24 GeV beam. (b) I-V curves measured at -15 °C for detectors A, B and D after 2x10^{14} protons/cm^2. See text for measurement details.

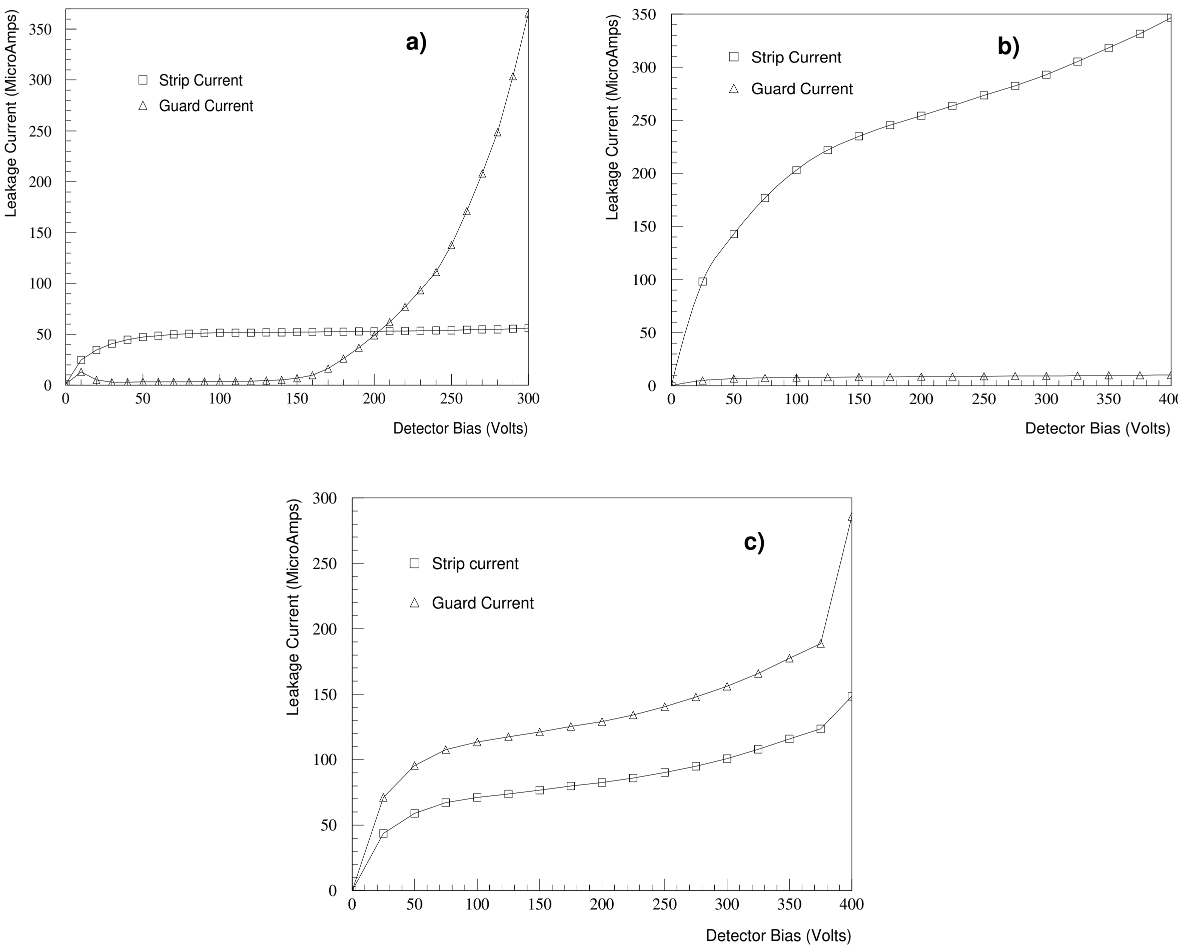

Figure 11-17 The current in the bulk and guard regions after irradiation to 2 x 10^{14} protons/cm^2
a) detector type A, b) detector type C, c) detector type E. The detectors C and E were measured at -10 °C.

A feature of the data that is not yet well understood is the behaviour of the current during and immediately after the very rapid PS irradiation. Some detectors showed high currents during irradiation. As illustrated in Figure 11-18, the current has a component that anneals very rapidly at room temperature. Further studies will be carried out in 1997 but, given the results of Figure 11-18, these effects appear unlikely to be of serious concern for the operation of detectors subjected to a much slower irradiation over a 10 year period within ATLAS. Since I_L should be dominated by bulk effects, the differing values of I_L in Figure 11-17 require further study.

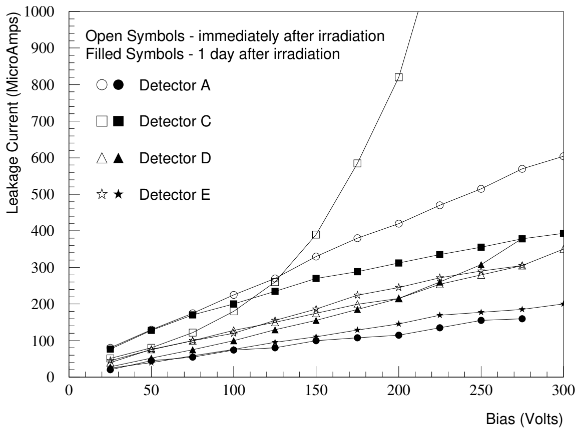

Figure 11-18 Detector leakage current for detectors A, C, D and E measured at -10 °C immediately after irradiation and following a 24-hour annealing period. The anneal time included a few hours at room temperature.

11.3.4.4 Detector C-V characteristics before and after irradiation

All detectors reach full depletion at voltages of ≤ 100V before irradiation. Figure 11-19 shows the variation of capacitance with bias voltage for an unirradiated detector of type C. Figure 11-20 shows the C-V curves for detector D irradiated to a fluence of 2×10^{14} protons/cm^2.

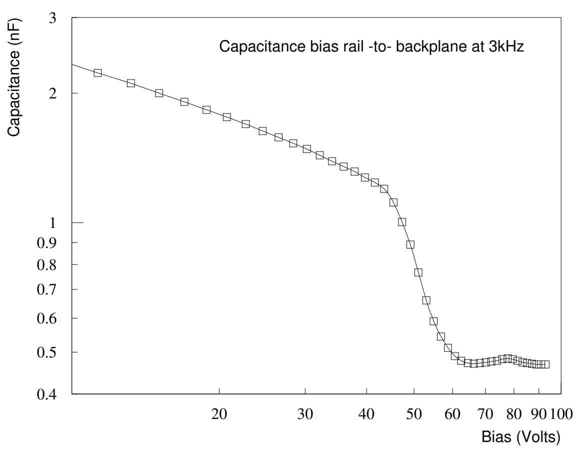

Figure 11-19 C-V dependence of an un-irradiated detector type C, at room temperature.

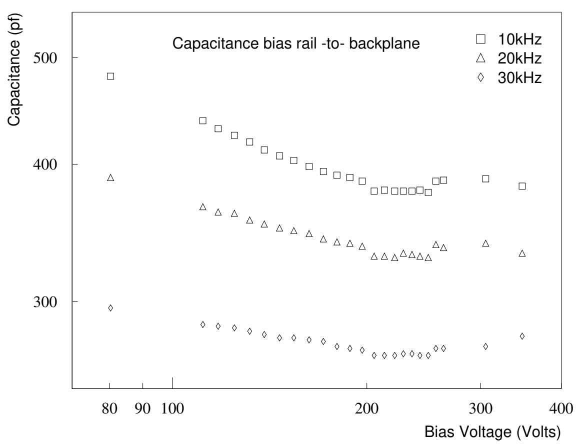

Figure 11-20 C-V dependence of an irradiated detector of type D, at an operating temperature of -10 °C

11.3.4.5 Performance of detectors with analogue readout before and after irradiation

The comparison of the pre- and post-irradiation performance of detectors was made using analogue readout electronics so that the full pulse-height information was available for the study. The FElix 128-channel readout chip [11-29, 11-30, 11-31] was used for these measurements. This has two distinct modes of operation; the *peak mode*, where the peaking time is ~75ns, and the *deconvoluted mode*, where the charge collected in 25ns is recovered from a pulse shape processor with some additional noise. Data were collected in each mode. The chips perform more stably and reliably in peak mode, but the deconvoluted data reveal whether any ballistic deficit is introduced at the speeds required for ATLAS operation.

Figure 11-21 indicates a single FElix chip attached and bonded to the detector on its ceramic board. The bonds between the aluminium tracks on the pitch adapter which is connected to the detector and those on the pitch adapter at the edge of the FElix readout board are remade when the detector is to be read out, and then broken again when the measurements are completed. The same FElix chip is therefore used to test several detectors, or several regions of 128 channels on the same detector (a complete detector has a 6x128 readout channels). The readout is not attached during irradiation, and only changes in the detector are studied.

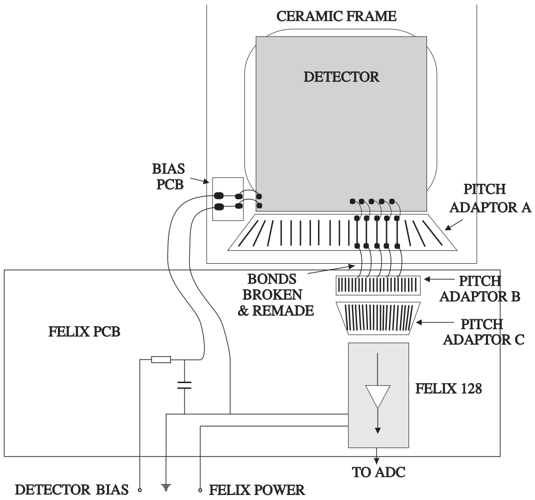

Figure 11-21 A schematic layout of a detector bonded to a FElix chip. The bonds between pitch adapters A and B are remade each time that the detector is connected for readout.

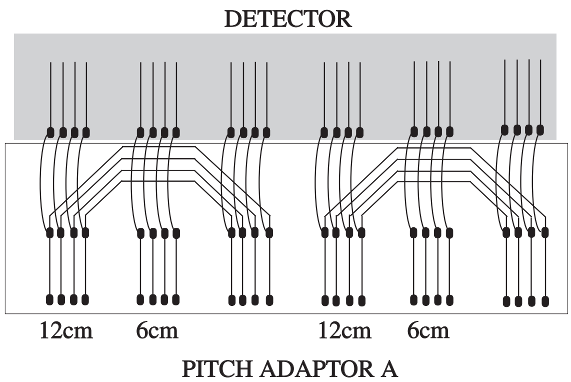

Figure 11-22 Schematic of a detail of the pitch adapter A showing the connection of detector strips to produce both 6 cm and 12 cm length strip readouts.

The noise seen in ~12cm long silicon strips is of primary interest. For this reason, the tracks on the pitch-adapter connected to the detector are arranged so that groups of ~6cm long detector strips are connected together at the readout end to form ~12cm long strips, as indicated in Figure 11-22. This is analogous to the baseline centre-tap configuration of a barrel module.

The noise values measured with the FElix readout system have common mode noise subtracted. Data were collected with a ^{106}Ru source to determine the charge collected from a minimum ionising particle. This was taken to be the total charge in a cluster of contiguous strips, with the following as the principal features of the cluster-finding algorithm:

- a cluster requires an initiator channel having S/N ratio of at least 4
- up to 5 strips are included in the cluster, provided the S/N value is at least 2 for each strip
- a S/N ratio of at least 5 is required for the complete cluster, and there must be only one cluster in the event.

The S/N value of the cluster is then defined as the sum of the S/N of the individual strips contributing to the cluster. The S/N requirement for the cluster initiator channel corresponds to a charge of close to 1fC for 12cm strips. This is the typical threshold setting for binary electronics, and thus the analogue initiator cut used in this analysis is close to the binary threshold cut that will operate with the SCT electronics.

Values measured for the noise and S/N for detectors before and after irradiation to 2 x 10^{14} protons/cm^2 are summarised in Table 11-11, with the irradiated detectors run at 300V bias. Also shown are the charge collection efficiencies of the irradiated detectors, normalised under the assumption that the unirradiated detectors operating at 150V collect 100% of the charge from the minimum ionising particles. The data for the irradiated detectors were taken at temperatures of -10 °C or -15 °C; there was found to be no significant variation of detector performance with temperature in the range -5 °C to -25 °C. It was also found that the value of the charge collection efficiency did not change significantly when the FElix chip was switched between peak or deconvoluted mode, that is, there was no evidence for ballistic deficit in the detectors. This is illustrated in Figure 11-23 using data from detector D.

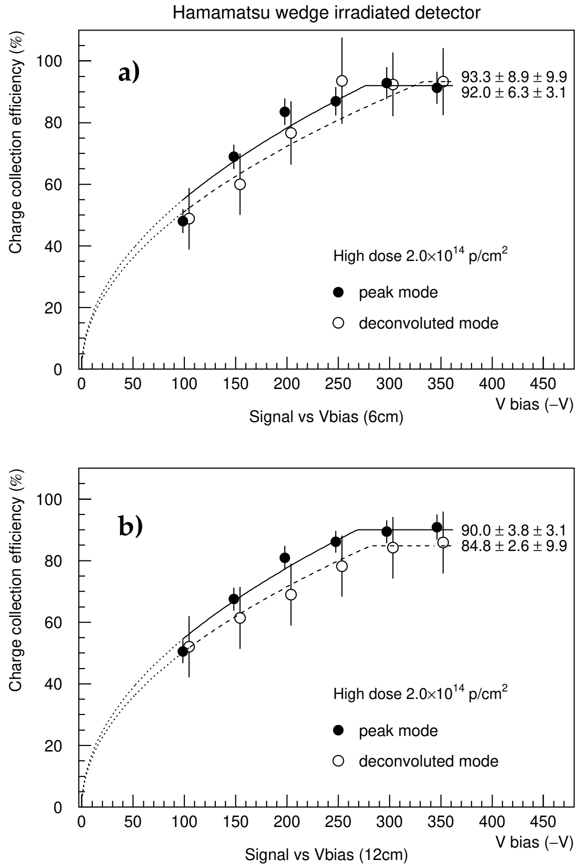

Figure 11-23 Charge collection for detector type D in peak and deconvoluted mode for a) 6cm and b) 12cm strips. (see text). Errors include the uncertainty of the absolute normalisation.

It can be seen from Table 11-11 that the irradiated detectors show satisfactory performance. Noise values ~1500 electrons r.m.s. seem to be achievable with detectors close to the final design, together with charge collection efficiencies approaching 90%. The results are illustrated in Figure 11-24 and Figure 11-25 which show the S/N distributions respectively before radiation for detector type B, and after irradiation for detector type C.

The noise and charge collection efficiency as a function of voltage after irradiation for four of the different design regions of detector C are shown in respectively Figure 11-26 and Figure 11-27. The charge collection as a function of volts for detectors of type A irradiated to 7.6 x 10^{13} protons/cm^2 and 2 x 10^{14} protons/cm^2. is shown in Figure 11-28; it can be seen that the data fit reasonably to a $\sqrt{V}$ dependence before the plateau of the maximum charge collection efficiency. This plateau begins at a bias of about 280V after a fluence of 2x10^{14} protons/cm^2 for the 300 µm thick devices.

The noise and charge collection efficiency data of the different regions of the irradiated detector C have provided input to the choice of the final *p*-stop design for the detectors to be prototyped in 1997. This is discussed further in Section 11.3.4.7 below.

In addition to noise and charge collection, an important property of a detector after irradiation is the quality of the strip readout, that is, the number of strips that are too noisy to be useful and

Table 11-11 Noise, signal:noise and charge collection efficiency measurements for different detectors using both the peak and deconvoluted modes of the FElix chip. The noise is in units of Ke-, with the value for 6cm strips followed by that for 12cm detector strips. The post-irradiation (to 2x10^{14} protons/cm^2) values were measured at 300V bias.

Detector Label	A	B	C Region 2	D	E
Pre-irradiation					
FElix noise- peak	0.87, 1.23	0.79, 1.16	-	0.70, 0.94	-
FElix noise- deconvoluted	1.40, 1.65	-	-	-	-
S/N (peak mode)	29,21	28,20	-	31, 24	-
Post-irradiation					
FElix: noise peak	1.01, 1.55	1.05, 1.42	1.08, 1.47	1.13, 1.34	1.09, 1.57
FElix: noise deconvoluted	1.52, 2.03	1.30,1.62	-	1.30, 1.52	-
S/N(peak mode)	19, 14	21,16	19, 14	18, 15	18, 12 *
Charge collection efficiency in %(peak)	86	90	89	90	87 *

* detector thickness scaled to 300 μm

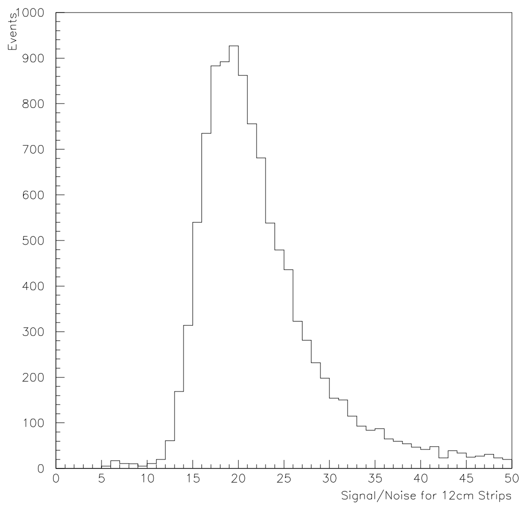

Figure 11-24 S/N distribution measured with a Ru^{106} source for 12 cm strips, detector B, before irradiation.

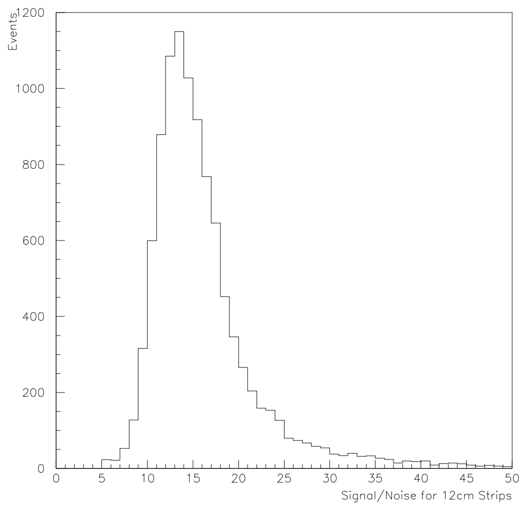

Figure 11-25 S/N distribution measure with a Ru^{106} source for 12 cm strips, detector C region 2, after irradiation to 2 x 10^{14} 24 GeV protons/cm^2.

the number of 'punch-through' channels where shorts have developed in the coupling dielectric. The measurements of 1996 have as yet yielded only limited information in this area because of the small number of detectors tested. In the case of detector C, of the 576 strips connected to readout, 4 had oxide shorts and 10 were noisy after irradiation to 2 x 10^{14} protons/cm^2, a total of 2.4% bad strips. An example of the noise for 128 channels of readout in region 2 of the detector is shown in Figure 11-29. This region contains the 4 punch-through channels, that once identified were disconnected and removed from the analysis. The percentage of bad strips found in this detector after irradiation is at the limit of acceptability; this issue is a priority for detector studies in 1997.

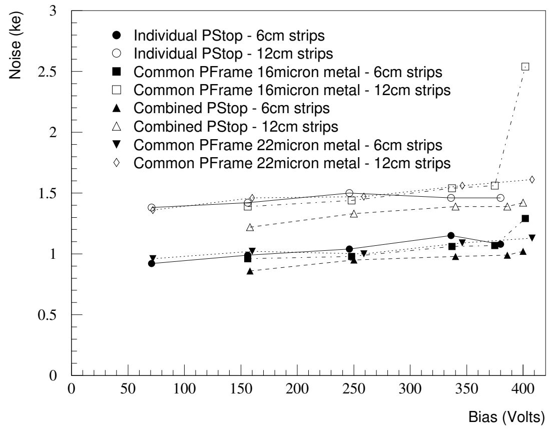

Figure 11-26 Peak mode noise for 4 separate regions of detector type C, after irradiation.

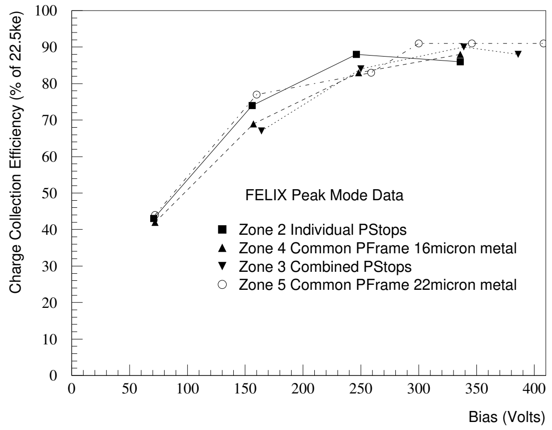

Figure 11-27 Charge collection efficiency for 4 different regions of detector type C, following irradiation.

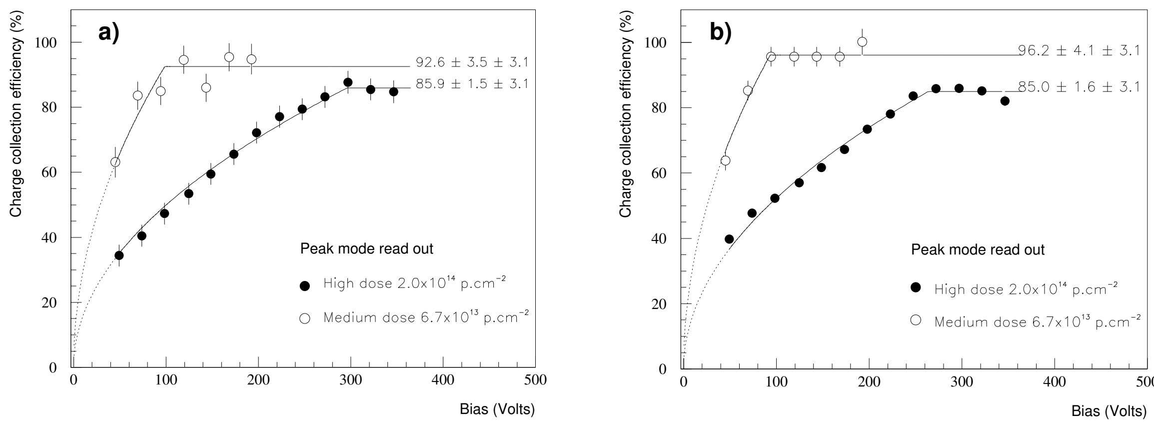

Figure 11-28 Charge collection efficiency as a function of bias for detector type A after irradiation to two different fluences, for (a) 6cm and (b) 12cm strips. The curves show a $\sqrt{V}$ fit to the data below depletion.

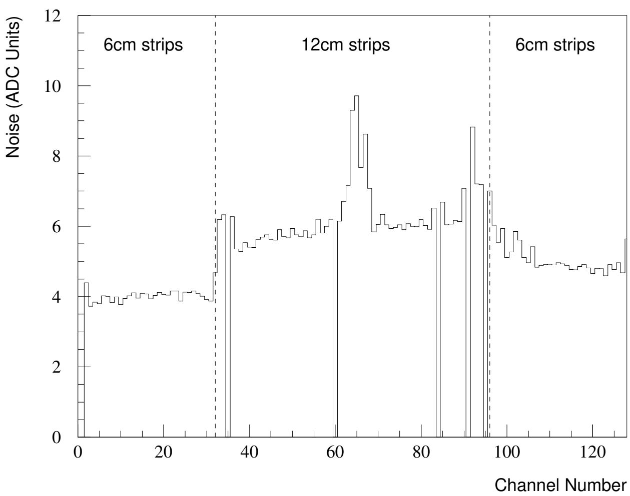

Figure 11-29 Common-mode corrected noise measured in peak mode for 128 channels of detector C after irradiation to 2 x 10^{14} protons/cm^2 in a 24 GeV beam, indicating the readout quality over regions of 6cm and 12cm long strips. The excess noise around channel 65 is a property of the particular FElix chip. The gain of this chip increases across the channels. Four of the zeros indicate punch-through channels (the other is due to the chip).

11.3.4.6 The detector biasing technique

The *n*-in-*n* detectors all have polysilicon biasing resistors specified in the range 1.5±0.5 MΩ. The alternative reach-through biasing technique was employed on MPI double-sided detectors which were irradiated at the PS at the same time as the baseline detectors. This technique was studied because of its potential cost impact. After a fluence of 2×10^{14} protons/cm^2 the MPI detectors showed excess noise when connected to the FElix readout system on both their *n* and *p* sides, with the foreseen shaping time of 25 ns. This depended on the detector temperature, and therefore current (becoming rapidly worse as the current increased), and also on the FElix shaping time. This is shown in Figure 11-30 where the data points were taken at -25 °C, -15 °C and -5 °C. After correcting for detector thickness, the S/N value for this detector is ~50% worse than that of a detector of type B at the highest current point in deconvoluted mode. This is attributed to the reach-through biasing. An increase in noise has recently been reported from reach-through biasing in the CDF experiment[11-32].

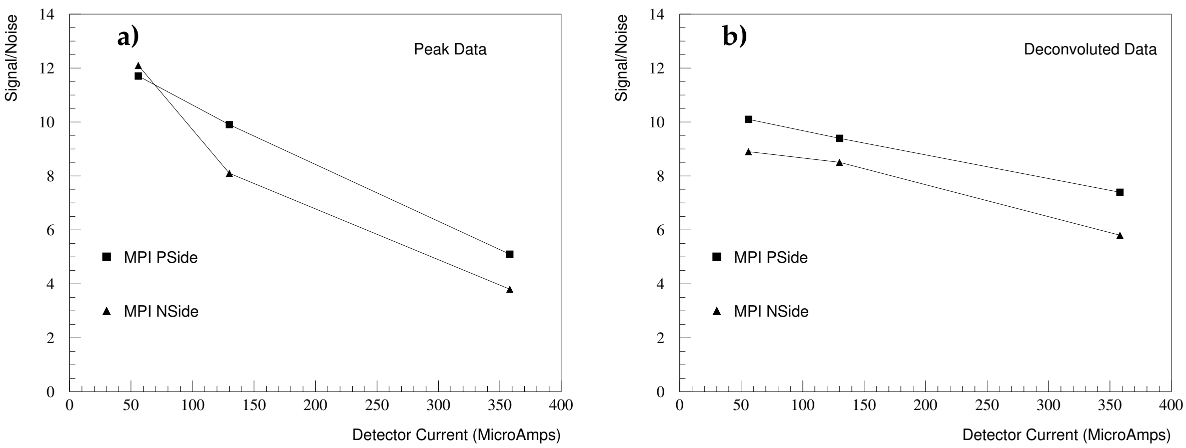

Figure 11-30 S/N values for the *p*- and *n*-sides of the double-sided detector as a function of the detector leakage current, for data taken in (a) peak mode and (b) deconvoluted mode. The 3 current values correspond to temperatures of -25 °C, -15 °C, and -5 °C.

The results confirm the choice of polysilicon resistor biasing for the ATLAS detectors.

11.3.4.7 The strip isolation technique

Results have been obtained for a variety of *p*-stop geometries, by measurements of the various detectors and from the different regions of the detector C. The relevant performance issues are detector noise, the fractional signal collected on a single strip (relevant to the single-strip threshold efficiency used in the binary electronics), and the high voltage stability of the detector before and after irradiation.

Measurements have been made using a source and in a KEK beam test of a centre-tap module consisting of 80 µm pitch type C detectors along with two end-tap modules for the forward region using type D detectors, all read out with binary electronics. The module design and subsequent results are presented in Section 11.5.3. Of the six different design regions of detector C, the occupancy, and thus the noise, is slightly lower in the 3rd region, which is formed from a combination of both the individual and common *p*-stop designs. It is also seen in Figure 11-26 that this same region has a marginally lower noise after irradiation, measured with analogue electronics. However, the design produces very crowded *p*-stop structures near the bond pads, which lead to increased fields at the *p*-stop edge and hence risk of micro-discharge at high bias.The simpler individual *p*-stop design of region 2 has therefore been chosen for ATLAS. This is also the *p*-stop design used in the type D wedge detector, which has satisfactory noise performance (Table 11-11) before and after irradiation.

Although test beam data indicate that the 2nd (individual *p*-stop) and 3rd (combined *p*-stop) regions have a smaller fraction of multi-hit strips (typically 10%), and a more uniform charge collection than other regions, these data are of marginal statistical significance.

The double-sided detector made by MPI used *p*-spray, as opposed to individual *p*-stops, for the *n*-strip isolation. These detectors show excellent I-V characteristics after irradiation, and have the advantage that the fields around the implants decrease with irradiation. It is planned to test the combination of *p*-spray and individual *p*-stops on a prototype subset of the 1997 *n*-in-*n* detectors (*p*-spray is an un-masked processing step) to see if this could provide improved I-V performance after irradiation together with acceptably low noise.

11.3.4.8 The edge termination technique

Extensive studies have been made of both field-plate and suitable multiple-guard-ring edge terminations for the detectors.

A radiation-tolerant multiple guard ring edge termination structure has been developed using both sides of the detector to protect against the possibility of avalanche breakdown arising from the increased depletion voltage after reverse annealing. The functionality of the floating guard design has been demonstrated at up to 650V bias prior to irradiation and up to 400V following exposure to up to 2×10^{14} protons/cm^2 [11-33].

For detectors biased at or below full depletion voltage, most of the potential is dropped by the guards on the side which forms the *p*-*n* junction with the bulk, but if the detector is well over-depleted the potential drop is shared by the guards on both sides. The sharing of potential across multiple guard rings ensures that extremely high bias voltages are necessary before the field intensity at any point within the structure is sufficient for the onset of avalanche breakdown. Figure 11-31 a) shows a ToSCA simulation of the floating guard potential distribution of an unirradiated detector, and Figure 11-31 b) shows the measured distribution from a real test structure. In Figure 11-31 a) and b) the potential drop is shared by the guards on both sides because the device is severely overdepleted. Figure 11-31 c) shows the measured *n*-side guard potential distribution after the device has been exposed to 1.5×10^{14} protons/cm^2 and has undergone significant reverse annealing. The depletion voltage in this case is ~200V and so more of the bias is dropped across the *n*-side guards. This guard ring design formed the basis of that used for detector D, with the satisfactory results already shown in Table 11-11.

The alternative field plate edge termination design [11-34] used in detectors B and C also performs well, as described in Section 11.3.4.3 and shown in Figure 11-24 to Figure 11-27. The space to be used for edge termination, rather than the choice between field plates and multiple guard rings, is the defined parameter in the detector specifications.

11.3.4.9 Operation of under-depleted detectors

One of the important properties of the *n*-in-*n* detector is its high efficiency when run substantially under-depleted after irradiation. This allows a system to be specified with a moderate maximum operating voltage (300 V). Results from test beam data show that the efficiency of an

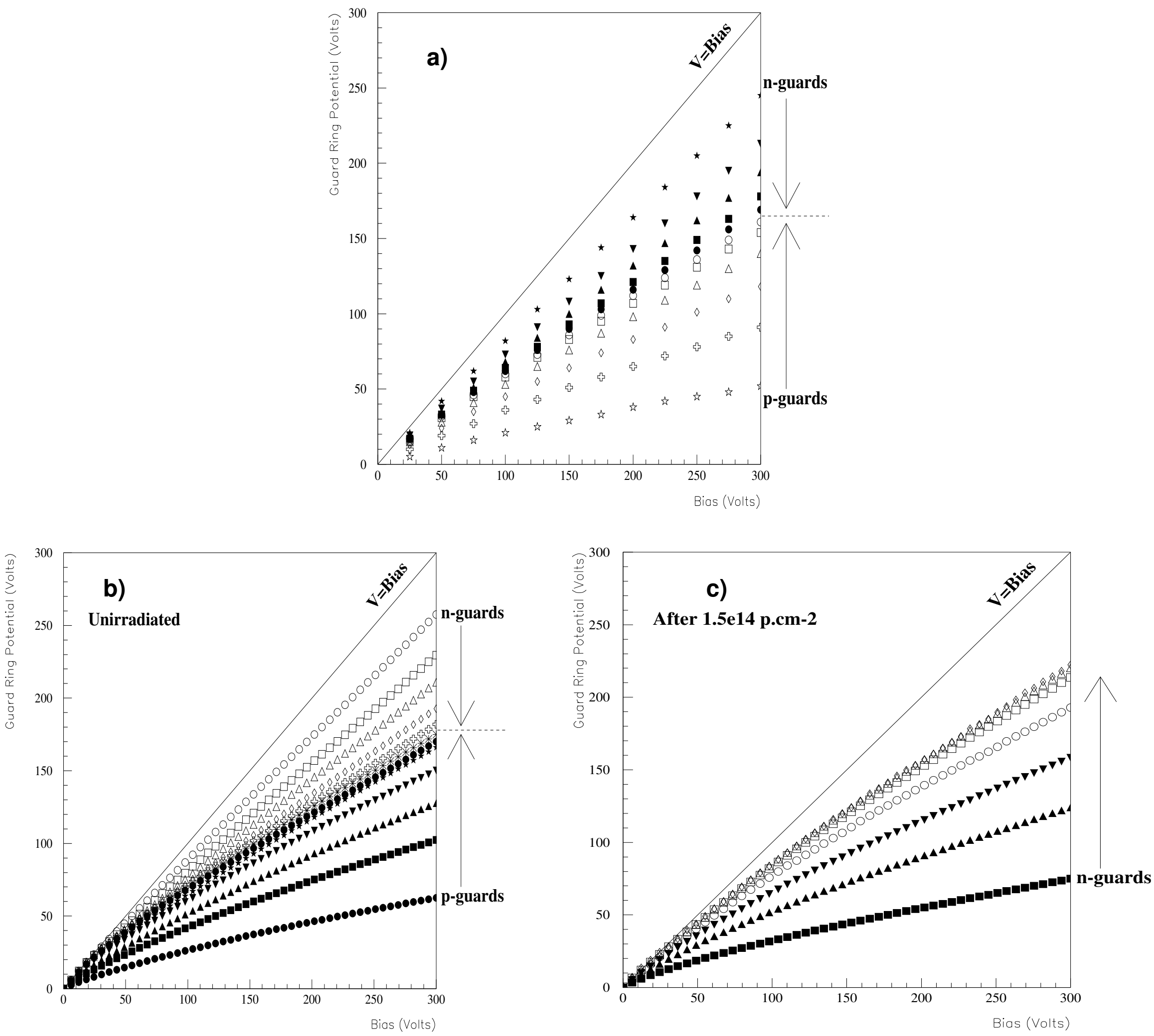

Figure 11-31 Potentials of each multiple guard ring as a function of bias, (a) as simulated using ToSCA for the *n*- and *p*-side guards, (b) as measured for an un-irradiated device with this guard ring structure, and (c) *n*-guard ring potentials measured for a device irradiated to 1.5 x 10^{14} 24 GeV protons/cm^2.

irradiated type B detector read out with binary electronics is still above 95% when operated at a bias of 150 V, which was only half the depletion voltage. This can be seen in Figure 11-32 from the data for the module ATT7 taken with the standard ATLAS binary electronic threshold setting equivalent to 1 fC. This module was irradiated to 10^{14} n_{eq}/cm^2 (equivalent) and had an annealing history giving a measured full depletion voltage of 290 V.

11.3.4.10 Summary of prototype results

ATLAS has studied full-sized prototype *n*-in-*n* detectors from a range of manufacturers. They perform well before irradiation and results after their exposure to 24 GeV proton fluences of 2x10^{14} particles/cm^2 appear satisfactory. These results are, however, based on measurements of limited statistics, and significantly higher statistics are required from tests of the detectors being made in 1997.

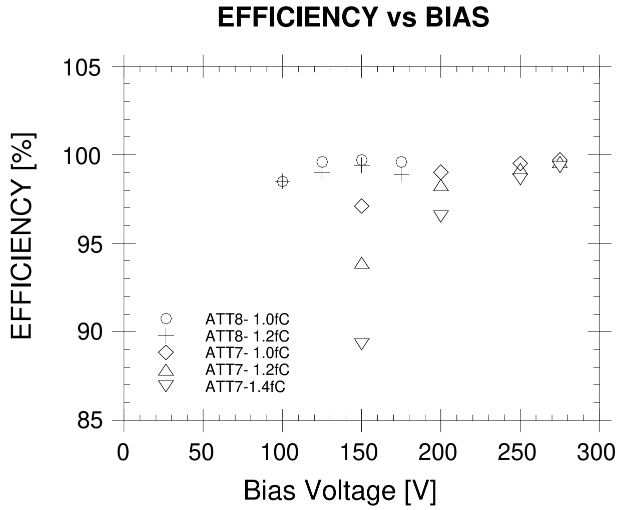

Figure 11-32 Efficiency of an unirradiated module (ATT8) and an irradiated module (ATT7) made from type B detectors as a function of bias voltage and binary threshold setting. The depletion voltage of ATT7 is 290V.

11.3.5 References

11-18 A. Ferrari, private communication.

11-19 E. Fretwurst et al., Reverse annealing of the effective purity concentration and long-term operational scenario for silicon detectors in future Collider experiments, Nucl. Instr. Methods A342 (1994), 119.
A. Chilingarov et al., Radiation Studies and Operational Projections in the ATLAS Inner Tracker, Nucl. Instr. Methods A360 (1995) 432-437.

11-20 H. Feik, private communication.

11-21 G. Lindstroem, private communication.

11-22 P.P. Allport, ATLAS Specifications for Silicon Microstrip Detectors, ATLAS-INDET-NO-164.

11-23 Micron Semiconductor Ltd., 1 Royal Buildings, Marlborough Road, Lancing, Sussex BN15 8UN, England, UK.

11-24 Hamamatsu Photonics K.K. 1126-1 Ichino-Cho, Hamamatsu City, Japan.

11-25 CSEM, Centre Suisse d'Electro et Micro-Technique, Maladiere 71-CP41, CH-2000 Neuchatel, Switzerland.

11-26 SINTEF, P.O. Box 124, Blindern, N-0314 Oslo, Norway.

11-27 Max Plank Institut fur Physik, Postfach 401212, Foehringer Ring 6, D-80805, Munich, Germany.

11-28 Faculty of Physics, Moscow State University, 119 899 Moscow, Russia.

11-29 S. Gadomski et al., Fast and Low Noise FrontEnd Electronics for Silicon Detectors at LHC, Nucl. Instr. Methods A351 (1994), 201-207.

11-30 W. Dabrowski, Development of Readout chips for the ATLAS Semiconductor Tracker, Nucl. Instr. Methods A383 (1996) 179-189.

11-31 J. Beringer et al., Atlas Test Beam Results, Nucl. Instr. Methods A383 (1996), 116-123.

11-32 P. Azzi et al., Radiation Damage at CDF with SVX', Nucl. Instr. Methods A383 (1996), 155-158.

11-33 G.A.Beck et al, "Radiation-Tolerant Breakdown of Silicon Detectors Using Multiple Float ing Guard Rings", accepted for publication in Nucl. Instr. and Methods.

11-34 T. Ohsugi et al., Micro-discharge at strip edge of silicon microstrip sensors, Nucl. Instr. Methods A383 (1996), 116-123.